ACS Energy LETTERS

http://pubs.acs.org/journal/aelccp

Ultrastable All-Solid-State Sodium Rechargeable Batteries

Jing Yang, Gaozhan Liu, Maxim Avdeev, Hongli Wan, Fudong Han, Lin Shen, Zheyi Zou, Siqi Shi,* Yong-Sheng Hu,* Chunsheng Wang,* and Xiayin Yao*

Cite This: *ACS Energy Lett.* 2020, 5, 2835−2841

Read Online

ACCESS | Metrics & More | Article Recommendations | Supporting Information

ABSTRACT: The insufficient ionic conductivity of oxide-based solid electrolytes and the large interfacial resistance between the cathode material and the solid electrolyte severely limit the performance of room-temperature all-solid-state sodium rechargeable batteries. A NASICON solid electrolyte $Na_{3.4}Zr_{1.9}Zn_{0.1}Si_{2.2}P_{0.8}O_{12}$, with superior room-temperature conductivity of 5.27×10^{-3} S cm^{-1}, is achieved by simultaneous substitution of Zr^{4+} by aliovalent Zn^{2+} and P^{5+} by Si^{4+} in $Na_3Zr_2Si_2PO_{12}$. The bulk conductivity and grain boundary conductivity of $Na_{3.4}Zr_{1.9}Zn_{0.1}Si_{2.2}P_{0.8}O_{12}$ are nearly 20 times and almost 50 times greater than those of pristine $Na_3Zr_2Si_2PO_{12}$, respectively. The FeS_2||polydopamine-$Na_{3.4}Zr_{1.9}Zn_{0.1}Si_{2.2}P_{0.8}O_{12}$||Na all-solid-state sodium batteries, with a polydopamine modification thin layer between the solid electrolyte and the cathode, maintain a high reversible capacity of 236.5 mAh g^{-1} at a 0.1 C rate for 100 cycles and a capacity of 133.1 mAh g^{-1} at 0.5 C for 300 cycles, demonstrating high performance for all-solid-state sodium batteries.

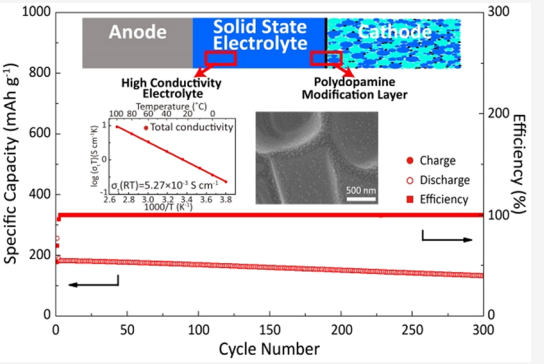

Because of the abundance and low cost of sodium resources, sodium-ion batteries are promising for large-scale storage and power grid applications.[1] All-solid-state sodium batteries using nonflammable solid electrolyte can achieve long cycling stability and high energy density because of the possibility of directly using metallic sodium anode and high-voltage cathodes.[2] Solid electrolytes are crucial components in all-solid-state sodium batteries. Among them, NASICON-structured electrolytes with composition of $Na_{1+x}Zr_2Si_xP_{3-x}O_{12}$ ($0 \le x \le 3$) attracted great interest because of good thermal and chemical stability.[3] The bulk ionic conductivity of the NASICON-structured electrolytes has been effectively enhanced via aliovalent substitution by modifying the bottleneck sizes of Na^+ migration channels and increasing the Na^+ concentration,[1,4−9] and the grain boundary conductivity has also been improved by material densification.[10,11] In addition, structure control through substitution is also essential in improving the conductivity.[12] Currently, the modification of $Na_{1+x}Zr_2Si_xP_{3-x}O_{12}$ ($0 \le x \le 3$) focuses on $Na_3Zr_2Si_2PO_{12}$-based material,[4,13−16] because the monoclinic NASICON phase ($1.8 \le x \le 2.2$) exhibits superior conductivity in comparison to the rhombohedral NASICON phase.[17,18] Further refining the composition of $Na_3Zr_2Si_2PO_{12}$ by substitution of P^{5+} by Si^{4+} and Zr^{4+} by low-valence anion can potentially further enhance the ionic conductivity, but this has not been systematically investigated.

In addition to the high conductivities of the solid electrolytes, the interfacial resistance between solid electrolytes and electrode is also crucial to achieve high performance for all-solid-state sodium batteries. The insufficient solid−solid contact between rigid solid electrolyte and electrode induces a high interfacial resistance.[19] Moreover, the volume expansion and shrinkage of active materials during charge−discharge cycles also cause structural failure and resistance increase, leading to accelerated capacity decay,[20] especially in cathodes with three-dimensional volume changes. A straightforward solution is to introduce an interlayer or interphase with good stability and intimate contact with electrode and electrolyte.[13−15]

In this work, $Na_{3.4}Zr_{1.9}Zn_{0.1}Si_{2.2}P_{0.8}O_{12}$ dense solid electrolyte with a high room-temperature sodium ionic conductivity of 5.27×10^{-3} S cm^{-1} is synthesized and a polydopamine (PDA) modification buffer layer is constructed, which lead to ultrastable all-solid-state sodium rechargeable batteries. $Na_{3.2+2x}Zr_{2-x}Zn_xSi_{2.2}P_{0.8}O_{12}$ (x = 0, 0.05, 0.1, 0.15) materials with different Zn content and pristine $Na_3Zr_2Si_2PO_{12}$ were

Received: July 4, 2020
Accepted: August 11, 2020
Published: August 11, 2020

Downloaded via UNIV OF MARYLAND COLG PARK on August 21, 2020 at 12:43:31 (UTC).
See https://pubs.acs.org/sharingguidelines for options on how to legitimately share published articles.

© XXXX American Chemical Society

https://dx.doi.org/10.1021/acsenergylett.0c01432
ACS Energy Lett. 2020, 5, 2835−2841

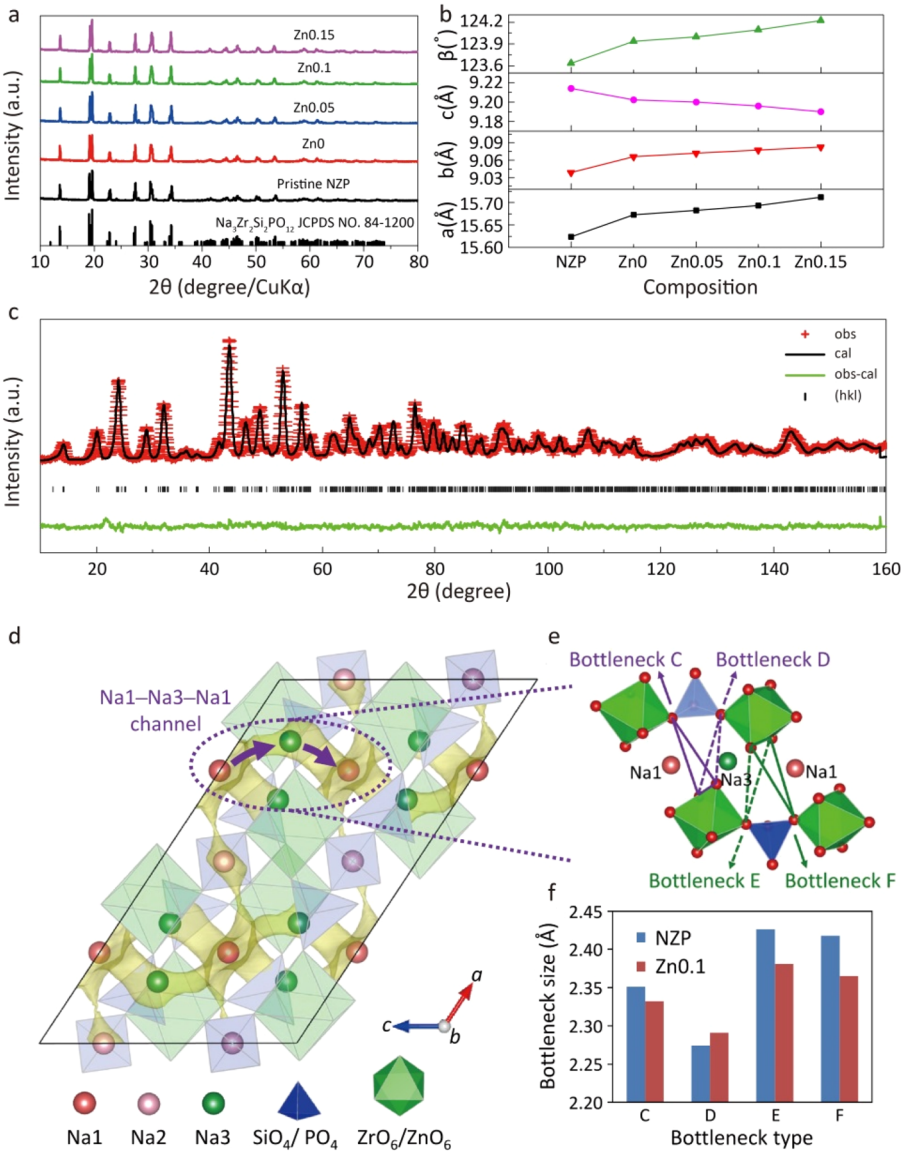

Figure 1. (a) XRD patterns of Zn0, Zn0.05, Zn0.1, Zn0.15, and pristine NZP. (b) Unit cell parameters of Zn0, Zn0.05, Zn0.1, Zn0.15, and pristine NZP. (c) The room-temperature NPD data of Zn0.1. Red crosses and black and green solid lines are experimental and calculated data and their difference, respectively. The tick marks show peak positions for the NASICON phase. (d) BVEL maps of NZP system with isosurfaces drawn at the 1.6 eV level above E_{min}. The rose, pink, and green spheres represent Na1, Na2, and Na3 sites, respectively. The purple arrows show one Na1−Na3−Na1 channel in the *bc* plane of the NZP unit cell. (e) Location of bottlenecks C, D, E, and F in Na1−Na3−Na1 channel. (f) Comparisons of size of different bottlenecks in Na1−Na3−Na1 channel for NZP system and Zn0.1 system.

synthesized at 1250 °C in pure oxygen through solid-state reaction. Henceforth, $Na_{3.2}Zr_2Si_{2.2}P_{0.8}O_{12}$, $Na_{3.3}Zr_{1.95}Zn_{0.05}Si_{2.2}P_{0.8}O_{12}$, $Na_{3.4}Zr_{1.9}Zn_{0.1}Si_{2.2}P_{0.8}O_{12}$, $Na_{3.5}Zr_{1.85}Zn_{0.15}Si_{2.2}P_{0.8}O_{12}$, and $Na_3Zr_2Si_2PO_{12}$ are denoted as Zn0, Zn0.05, Zn0.1, Zn0.15, and pristine NZP, respectively. The difference between Zn0 and NZP is the higher Si/P atomic ratio of 2.75 in Zn0 than that (2.0) in NZP, reflecting the impact of substitution of P^{5+} by Si^{4+} in the property. As shown in the X-ray diffraction (XRD) patterns in Figure 1a, at a low substitution of <0.15, all Zn0, Zn0.05, Zn0.1, Zn0.15, and pristine NZP electrolytes possess the same monoclinic ($C2/c$) NASICON main phase, indicating no crystalline structure change. However, when Zn concentration is greater than 0.3, the crystalline structure of $Na_{3.8}Zr_{1.7}Zn_{0.3}Si_{2.2}P_{0.8}O_{12}$ and $Na_4Zr_{1.6}Zn_{0.4}Si_{2.2}P_{0.8}O_{12}$ (x = 0.3 and x = 0.4, termed Zn0.3 and Zn0.4) changed from monoclinic to an undesirable rhombohedral structure (Figure S1). In addition, a Zn-containing phase $Na_9Zn_3(PO_4)_5$ is also detected. The unit cell parameters reveal that the lattice parameters of a, b, and β angle increase and c decreases as Zn doping concentration increases (Figure 1b and Table S1). The substitution of Zr^{4+} with Zn^{2+} is further confirmed with the Rietveld analysis of the neutron powder diffraction (NPD) data (Figure 1c). As shown in Figures 1c and S2 and Table S2, Zn^{2+} and Zr^{4+} occupied the same 8f octahedral site in the unit cells of all samples. In addition, no element segregation is observed in the Zn0.1 sample according to the scanning transmission electron microscopy energy dispersive X-ray spectroscopy (STEM-EDS) result (Figure S3), further confirming that Zn^{2+} is incorporated in the NASICON main phase. All the characterizations confirmed that the Zn^{2+} substituted Zr^{4+}. Moreover, no difference could be found in peak intensities and peak positions between the XRD

https://dx.doi.org/10.1021/acsenergylett.0c01432
ACS Energy Lett. 2020, 5, 2835−2841

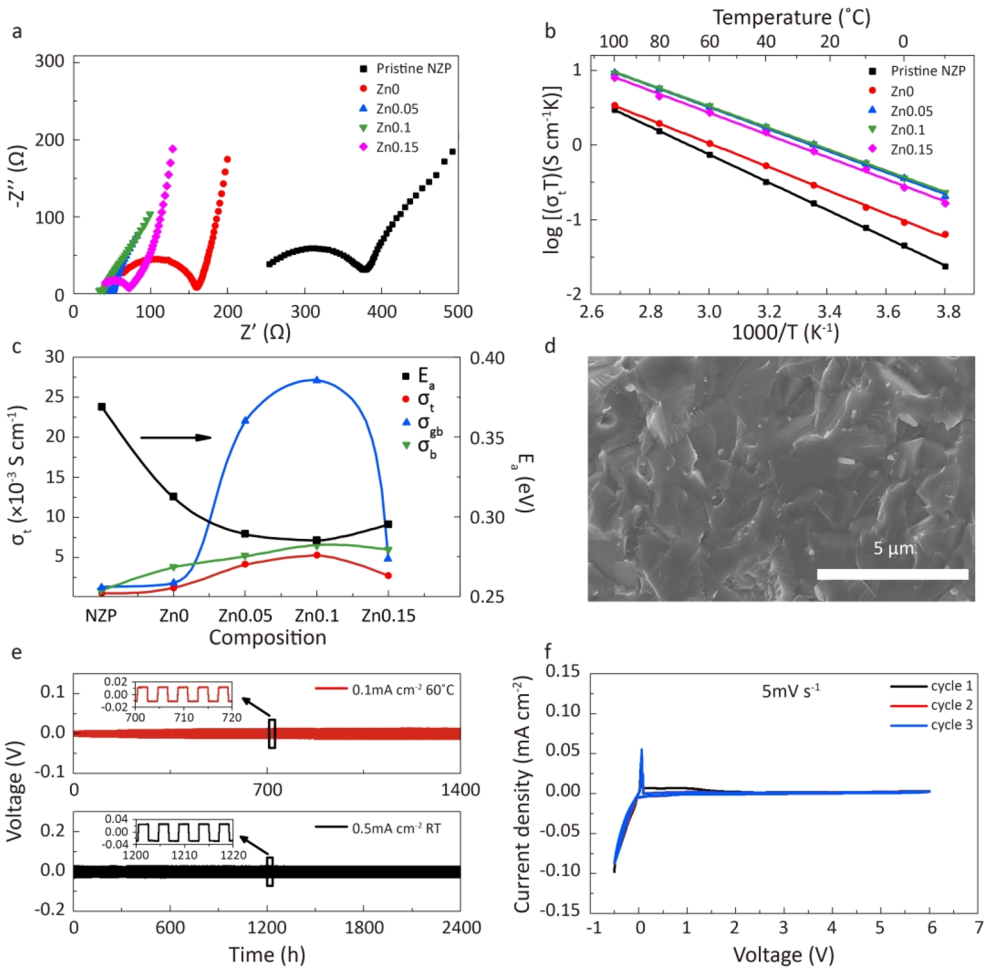

Figure 2. (a) Room-temperature impedance plots of Zn0, Zn0.05, Zn0.1, Zn0.15, and pristine NZP sintered at 1250 °C in pure oxygen. (b) Arrhenius plots of Zn0, Zn0.05, Zn0.1, Zn0.15, and pristine NZP sintered at 1250 °C in pure oxygen. (c) Conductivities and activation energies of Zn0, Zn0.05, Zn0.1, Zn0.15, and pristine NZP. (d) Cross-sectional morphology of Zn0.1 sintered at 1250 °C in pure oxygen. (e) Galvanostatic cycling of the Na/Zn0.1/Na cell. (f) Cyclic voltammetry curve of Zn0.1 sample.

patterns of Zn0.1 sample sintered in oxygen and ambient air (Figure S4).

The geometric analysis which was based on the NPD data suggested that substitution of Zr^{4+} by Zn^{2+} enlarges the bottlenecks in the migration channels (Figure 1d-f). The main migration channels in the monoclinic NASICON-type structure are Na1−Na2−Na1 channel and Na1−Na3−Na1 channel. For both the Na1−Na2−Na1 and the Na1−Na3−Na1 channels, the Na^+ must migrate through four triangular bottlenecks. Each bottleneck consists of three O atoms of the framework. The bottlenecks in the Na1−Na2−Na1 and Na1−Na3−Na1 channels are designated by the symbols "A, B, B′, A′ " and "C, D, E, F", respectively (Figures S5 and 1e). The NPD characterization (Table S3) demonstrated that the sizes of the smallest bottlenecks in the Na1−Na3−Na1 channel (bottleneck D) in NZP and Zn0.1 electrolytes are larger than that in the Na1−Na2−Na1 channel (bottleneck B). However, both of them are smaller than the sum of the O^{2-} and Na^+ radii (about 2.35 Å according to the Shannon effective ionic radii table[21]). Thus, the diffusion of Na^+ in these systems is anisotropic, and Na^+ tends to migrate through the Na1−Na3−Na1 channels in the *bc* plane rather than through the Na1−Na2−Na1 channels along the [101] direction owning to the larger size of bottleneck D compared with bottleneck B, which agrees with the previous studies.[22] Notably, the size of the bottleneck D in Na1−Na3−Na1 channel is enlarged from 2.274 to 2.291 Å by Zn^{2+} substitution, as shown in Figure 1f. Furthermore, Zr^{4+} substitution by Zn^{2+} also increases the Na^+ content, which also increases the bulk conductivity of the monoclinic NASICON-type materials because of the enhancement of correlated migration.[22] Therefore, Zr^{4+} substitution by Zn^{2+} both modifies the size of the smallest bottleneck in Na1−Na3−Na1 channel and increases the Na^+ content in the system, which would lead to higher Na^+ conductivity.

The ionic conducting properties of $Na_{3.2+2x}Zr_{2-x}Zn_xSi_{2.2}P_{0.8}O_{12}$ electrolytes sintered at 1250 °C in pure oxygen were measured using electrochemical impedance spectroscopy (EIS). Figure 2a displays the room-temperature impedance plots, and Figure 2b shows the Arrhenius plots of Zn0, Zn0.05, Zn0.1, Zn0.15, and pristine NZP. The conductivities, activation energies, and relative densities are summarized in Figure 2c and Table S4. The higher conductivities (1.19×10^{-3} S cm^{-1}) of Zn0 electrolyte than that (5.22×10^{-4} S cm^{-1}) of the pristine NZP demonstrated that increasing the Si/P atomic ratio enhances the ionic conductivity. For the Zn^{2+} substitution of Zr^{4+}, the total conductivity of $Na_{3.2+2x}Zr_{2-x}Zn_xSi_{2.2}P_{0.8}O_{12}$ electrolytes reaches a maximum ionic conductivity of 5.27×10^{-3} S cm^{-1} for Zn0.1. The Zn^{2+}

https://dx.doi.org/10.1021/acsenergylett.0c01432
ACS Energy Lett. 2020, 5, 2835−2841

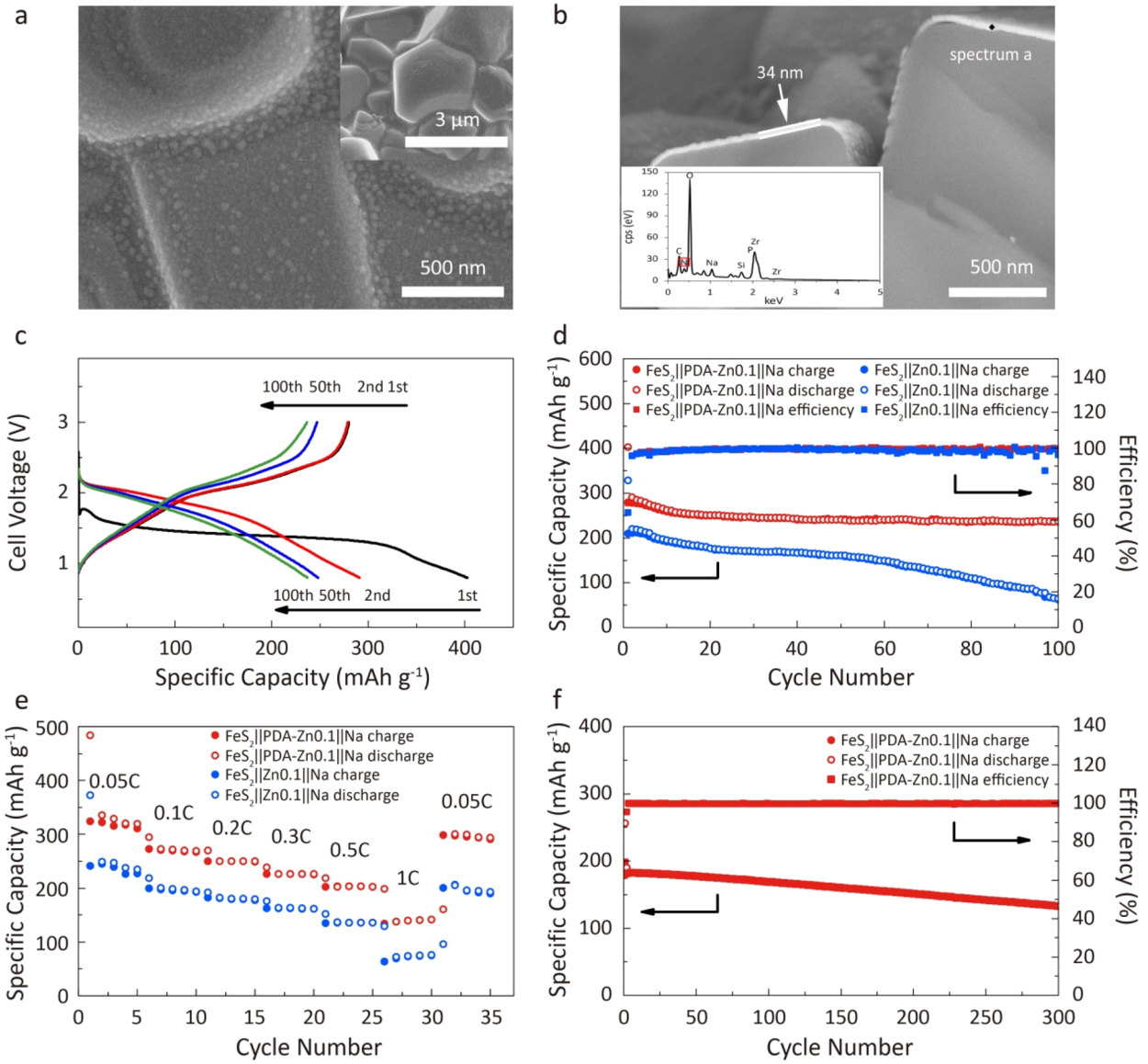

Figure 3. (a) Surface morphology of Zn0.1 pellet after PDA coating. (b) Cross-sectional SEM images of Zn0.1 pellet after PDA coating and the EDS result of the coating layer. (c) Charge−discharge curves and the cycling performance of FeS_2||PDA-Zn0.1||Na battery operated under a current of 0.1 C at 60 °C. (d) Cycling performance of FeS_2||PDA-Zn0.1||Na battery and FeS_2||Zn0.1||Na battery operated under a current of 0.1 C at 60 °C. (e) Rate performance of FeS_2||PDA-Zn0.1||Na battery and FeS_2||Zn0.1||Na battery operated at 60 °C. (f) Cycling performance of FeS_2||PDA-Zn0.1||Na battery operated under a current of 0.5 C at 60 °C.

substitution modifies the bottleneck sizes and improves the Na^+ transportation; in addition, the addition of Zn also promotes sintering densification and grain growth through liquid-phase sintering by forming a Zn-rich liquid phase and acceleration of the mass transport,[23] which is also beneficial for the conductivity enhancement. When temperature increases to 60 °C, the conductivity of Zn0.1 electrolyte can further enhance to 1.14×10^{-2} S cm^{-1} (Figure 2b). However, the ionic conductivity of the electrolytes decrease when Zn content exceeds 0.1 (Table S4), which might be caused by the expanded Na^+ migration bottlenecks beyond the optimal sizes and the high Na^+ concentration disrupting correlated transport.[5] In addition, owing to the good solubility and diffusivity of oxygen, the oxygen sintering atmosphere could facilitate the disappearance of intergranular pores via lattice diffusion or vacancy transport,[11] leading to high grain boundary ionic conductivity. As shown in Figure S6, Zn0.1 electrolyte sintered in the air shows pores and micro cracks along grain boundaries, while no pores are observed in the Zn0.1 electrolyte that was sintered in the oxygen (Figure 2d). As demonstrated in Figures S7−S9 and Tables S4−S6, the grain boundary conductivity (2.73×10^{-2} S cm^{-1}) of Zn0.1 electrolyte sintered in an oxygen environment is almost two times higher than that (1.53×10^{-2} S cm^{-1}) of samples sintered in ambient air and is nearly 50 times greater than that (5.57×10^{-4} S cm^{-1}) of pristine NZP sintered in ambient air. To our knowledge, the total conductivity of Zn0.1 is one of the highest among NASICON-structured Na-ion conductive oxide solid electrolytes reported in the literature[4,6,13,16,24] (Figure S10).

The stability of Zn0.1 electrolyte against metallic sodium was investigated using a symmetrical Na/Zn0.1/Na cell at a current density of 0.5 mA cm^{-2} and a capacity of 1.0 mAh cm^{-2} under room-temperature. As presented in Figure 2e, the Na plating/stripping in symmetrical Na/Zn0.1/Na cell remains stable for

https://dx.doi.org/10.1021/acsenergylett.0c01432
ACS Energy Lett. 2020, 5, 2835−2841

2400 h. Besides, when tested at 0.1 mA cm^{-2} and 60 °C, the potential polarization gradually increased during the initial Na plating/stripping and then stabilized after 800 h and remained stable up to 1400 h. The electrochemical window of Zn0.1 electrolyte is determined by cyclic voltammetry, and no peaks or noticeable oxidation current is observed up to 6 V (Figure 2f). After formation of a passivation layer during initial Na stripping and plating cycles, the Zn0.1 electrolyte shows excellent stability with sodium metal in the following cycles. However, the surface of the Zn0.1 electrolyte becomes rough after contact with sodium metal because of formation of solid electrolyte interphase. Nevertheless, the element distribution on the surface is still homogeneous and almost the same as the fresh state, suggesting negligible side reaction occurs on the surface of Zn0.1 pellet (Figure S11a). The electronic conductivity at room temperature is determined to be 4.7×10^{-9} S cm^{-1} by DC polarization measurement (Figure S11b), and the transference number is close to 1. The high ionic conductivity, the wide stability window, high stability against Na, and low electronic conductivity make Zn0.1 electrolyte a good candidate for all-solid-state sodium batteries.

To reduce the high interfacial resistance at the cathode/electrolyte interface in the all-solid-state sodium batteries, an air-stable PDA thin layer was coated on the surface of Zn0.1 electrolyte pellet through a facile *in situ* polymerization method. The powerful adhesion capability of elastic PDA layer ensures its strong binding on the surface of the Zn0.1 electrolyte pellet and intimate face-contact between the electrolyte and the cathode material[25] and provides the necessary flexibility to accommodate volumetric changes to maintain the interfacial contact and structural integrity during cycling. The charge-transfer interactions between *o*-benzoquinone and catechol units in PDA enabled the Na-ion transfer.[26] The surface morphology of Zn0.1 pellets before and after PDA coating is presented in Figures S12a and 3a, respectively. A continuous dense layer with evenly distributed small particles is formed on the surface of the electrolyte grains. Moreover, the gaps between the grains have been eliminated because of the PDA coating layer, resulting in the effectively increased contact area and interfacial contact. The thickness of the uniform coating layer is determined to be approximately 34 nm (Figure 3b). The EDS mapping demonstrated that the surface layer contains nitrogen, carbon, oxygen, sodium, silicon, zirconium, and phosphorus. The characteristic peak of the N−H stretching vibration centered at 1510 cm^{-1} in the Fourier transform infrared spectroscopy (FTIR) spectra (Figure S12b) and the existence of element nitrogen in EDS mapping further confirms the PDA coating layer.

The electrochemical performances of FeS_2||PDA-Zn0.1||Na all-solid-state batteries were evaluated at a current density of 0.1 C at 60 °C. For comparison, the performances of FeS_2||Zn0.1||Na all-solid-state batteries without PDA buffer layer were also evaluated under the same conditions (Figures S13 and 3d). As shown in Figure 3c,d, the FeS_2||PDA-Zn0.1||Na all-solid-state battery delivers a charge capacity of 279.9 mAh g^{-1} with a Coulombic efficiency of 69.54% in the initial charge−discharge cycle. The capacity slightly decays to 250 mAh g^{-1} within 15 cycles and then remains stable at 236.5 mAh g^{-1} after 100 cycles, which is much higher than that of PDA-absent FeS_2||Zn0.1||Na all-solid-state sodium battery with only 63.21 mAh g^{-1} capacity remaining at the 100th cycle. The low initial Coulombic efficiency and capacity fading before the 15th cycle is due to the phase transformation of FeS_2 (from pyrite FeS_2 to Na_xFeS_2[27]). The rate capability and long cycling stability of FeS_2||PDA-Zn0.1||Na all-solid-state batteries are further evaluated (Figure 3e,f). The FeS_2||PDA-Zn0.1||Na cell maintains high capacities of 311.3, 267.3, 249.3, 225.5, 202.7, and 141.6 mAh g^{-1} at the rates of 0.05, 0.1, 0.2, 0.3, 0.5, and 1 C, respectively, and recovers back to 291.1 mAh g^{-1} when the current density is reset to 0.05 C. By contrast, the PDA-absent FeS_2||Zn0.1||Na cell provides reversible capacities of only 226.9, 192.6, 178.2, 161.4, 136.1, and 75.5 mAh g^{-1} at 0.05, 0.1, 0.2, 0.3, 0.5, and 1 C, respectively, and a low capacity of only 189.9 mAh g^{-1} can be recovered at 0.05 C (Figure 3e). Moreover, the FeS_2||PDA-Zn0.1||Na all-solid-state battery also shows a long cycling stability. At a high current of 0.5 C, the FeS_2||PDA-Zn0.1||Na battery could deliver a reversible capacity of 133.1 mAh g^{-1} for 300 cycles with a capacity retention ratio of 73.3%, which is one of the best performances among all reported NASICON solid electrolyte-based all-solid-state batteries (Figure S14).[13,24,28−30]

The robustness of the PDA layer in combining the Zn0.1 electrolyte with FeS_2 cathode is witnessed by comparing the cross-sectional images of the cathode/electrolyte interface in the FeS_2||PDA-Zn0.1||Na and FeS_2||Zn0.1||Na cells after 100 cycles at 0.1 C and 60 °C. As illustrated in Figure S15a,c, the FeS_2 composite cathode is in close contact with the Zn0.1 pellet before cycling in both cells. Severe structural failure is observed at the the cathode/electrolyte interface in FeS_2||Zn0.1||Na battery after cycling (Figure S15b), resulting in capacity decay. By contrast, FeS_2||PDA-Zn0.1||Na battery shows only a few pores, and an intimate interface is still maintained (Figure S15b), which enables the Na^+ transfer at the interface and thus the favorable cycling performance and rate capability.

In summary, dense $Na_{3.4}Zr_{1.9}Zn_{0.1}Si_{2.2}P_{0.8}O_{12}$ NASICON solid electrolytes with a record high ionic conductivity of 5.27×10^{-3} S cm^{-1} were synthesized by simultaneous substitution of P^{5+} with Si^{4+} and Zr^{4+} with Zn^{2+} and sintering in oxygen atmosphere. $Na_{3.4}Zr_{1.9}Zn_{0.1}Si_{2.2}P_{0.8}O_{12}$ electrolytes were evaluated in FeS_2||PDA-$Na_{3.4}Zr_{1.9}Zn_{0.1}Si_{2.2}P_{0.8}O_{12}$||Na all-solid-state cells in which a PDA layer with strong bonding to $Na_{3.4}Zr_{1.9}Zn_{0.1}Si_{2.2}P_{0.8}O_{12}$ electrolyte was employed to ensure intimate contact and to accommodate volume changes of the cathode material during cycling. The obtained all-solid-state battery exhibits improved cycling capacity of 236.5 mAh g^{-1} after 100 cycles at 0.1 C rate and high rate cycling stability with a capacity of 133.1 mAh g^{-1} after 300 cycles at 0.5 C. This modification strategy could be widely applied to other high energy density solid-state battery systems.

■ ASSOCIATED CONTENT

Supporting Information

The Supporting Information is available free of charge at https://pubs.acs.org/doi/10.1021/acsenergylett.0c01432.

Experimental section; XRD, NPD, SEM, and EIS measurements for different solid electrolyte materials; STEM-EDS and DC polarization measurement for Zn0.1 sample; EDS measurement for Zn0.1 sample before and after contact with sodium; unit cell parameters of different solid electrolyte materials; structural parameters of different solid electrolyte materials; BVEL analysis and the comparison of bottleneck sizes; conductivities, activation energies, and relative densities of different solid electrolyte materials; FTIR measurement for Zn0.1 pellet with and without PDA layer; charge−discharge curves of FeS_2||Zn0.1||Na all-solid-state battery; compar-

https://dx.doi.org/10.1021/acsenergylett.0c01432
ACS Energy Lett. 2020, 5, 2835−2841

ison of conductivities and battery performances reported in the literature and in this work; cross-sectional images of the cathode/electrolyte interface before and after cycling (PDF)

AUTHOR INFORMATION

Corresponding Authors

Siqi Shi − *School of Materials Science and Engineering, Shanghai University, Shanghai 200444, P.R. China;* orcid.org/0000-0001-8988-9763; Email: sqshi@shu.edu.cn

Yong-Sheng Hu − *Center of Materials Science and Optoelectronics Engineering, University of Chinese Academy of Sciences, Beijing 100049, P.R. China; Key Laboratory for Renewable Energy Beijing Key Laboratory for New Energy Materials and Devices, Institute of Physics, Chinese Academy of Sciences, Beijing 100190, P.R. China;* orcid.org/0000-0002-8430-6474; Email: yshu@aphy.iphy.ac.cn

Chunsheng Wang − *Department of Chemical and Biomolecular Engineering, University of Maryland, College Park, Maryland 20742, United States;* orcid.org/0000-0002-8626-6381; Email: cswang@umd.edu

Xiayin Yao − *Ningbo Institute of Materials Technology and Engineering, Ningbo 315201, P.R. China; Center of Materials Science and Optoelectronics Engineering, University of Chinese Academy of Sciences, Beijing 100049, P.R. China;* orcid.org/0000-0002-2224-4247; Email: yaoxy@nimte.ac.cn

Authors

Jing Yang − *Ningbo Institute of Materials Technology and Engineering, Ningbo 315201, P.R. China*

Gaozhan Liu − *Ningbo Institute of Materials Technology and Engineering, Ningbo 315201, P.R. China; Center of Materials Science and Optoelectronics Engineering, University of Chinese Academy of Sciences, Beijing 100049, P.R. China*

Maxim Avdeev − *Australian Nuclear Science and Technology Organization, Lucas Heights, NSW 2234, Australia;* orcid.org/0000-0003-2366-5809

Hongli Wan − *Ningbo Institute of Materials Technology and Engineering, Ningbo 315201, P.R. China; Center of Materials Science and Optoelectronics Engineering, University of Chinese Academy of Sciences, Beijing 100049, P.R. China*

Fudong Han − *Department of Chemical and Biomolecular Engineering, University of Maryland, College Park, Maryland 20742, United States*

Lin Shen − *Ningbo Institute of Materials Technology and Engineering, Ningbo 315201, P.R. China; Center of Materials Science and Optoelectronics Engineering, University of Chinese Academy of Sciences, Beijing 100049, P.R. China*

Zheyi Zou − *School of Materials Science and Engineering, Shanghai University, Shanghai 200444, P.R. China*

Complete contact information is available at: https://pubs.acs.org/10.1021/acsenergylett.0c01432

Notes

The authors declare no competing financial interest.

ACKNOWLEDGMENTS

The work was supported by funding from the National Key R&D Program of China (Grant No. 2016YFB0901500), National Natural Science Foundation of China (Grant Nos. 51872303, U1964205, and 11874254), Zhejiang Provincial Natural Science Foundation of China (Grant Nos. LD18E020004 and LY18E020018), and Youth Innovation Promotion Association CAS (2017342).

REFERENCES

(1) Lu, Y.; Li, L.; Zhang, Q.; Niu, Z.; Chen, J. Electrolyte and interface engineering for solid-state sodium batteries. *Joule* **2018**, *2*, 1747−1770.

(2) Kim, J.-J.; Yoon, K.; Park, I.; Kang, K. Progress in the development of sodium-ion solid electrolytes. *Small Methods* **2017**, *1*, 1700219−1700230.

(3) Jian, Z.; Hu, Y.-S.; Ji, X.; Chen, W. NASICON-structured materials for energy storage. *Adv. Mater.* **2017**, *29*, 1601925−1601940.

(4) Song, S.; Duong, H. M.; Korsunsky, A. M.; Hu, N.; Lu, L. A Na^+ superionic conductor for room-temperature sodium batteries. *Sci. Rep.* **2016**, *6*, 32330−32339.

(5) Guin, M.; Tietz, F. Survey of the transport properties of sodium superionic conductor materials for use in sodium batteries. *J. Power Sources* **2015**, *273*, 1056−1064.

(6) Samiee, M.; Radhakrishnan, B.; Rice, Z.; Deng, Z.; Meng, Y. S.; Ong, S. P.; Luo, J. Divalent-doped $Na_3Zr_2Si_2PO_{12}$ natrium superionic conductor: Improving the ionic conductivity via simultaneously optimizing the phase and chemistry of the primary and secondary phases. *J. Power Sources* **2017**, *347*, 229−237.

(7) Bogusz, W.; Krok, F.; Jakubowski, W. Influence of doping on some physical properties of NASICON. *Solid State Ionics* **1983**, *9−10*, 803−807.

(8) Jolley, A. G.; Cohn, G.; Hitz, G. T.; Wachsman, E. D. Improving the ionic conductivity of NASICON through aliovalent cation substitution of $Na_3Zr_2Si_2PO_{12}$. *Ionics* **2015**, *21*, 3031−3038.

(9) Shi, S.; Gao, J.; Liu, Y.; Zhao, Y.; Wu, Q.; Ju, W.; Ouyang, C.; Xiao, R. Multi-scale computation methods: Their applications in lithium-ion battery research and development. *Chin. Phys. B* **2016**, *25*, 018212.

(10) Lee, J.-S.; Chang, C.-M.; Lee, Y. I. L.; Lee, J.-H.; Hong, S.-H. Spark Plasma Sintering (SPS) of NASICON Ceramics. *J. Am. Ceram. Soc.* **2004**, *87*, 305−307.

(11) Li, Y.; Wang, Z.; Li, C.; Cao, Y.; Guo, X. Densification and ionic-conduction improvement of lithium garnet solid electrolytes by flowing oxygen sintering. *J. Power Sources* **2014**, *248*, 642−646.

(12) Jolley, A. G.; Taylor, D. D.; Schreiber, N. J.; Wachsman, E. D. Structural investigation of monoclinic-rhombohedral phase transition in $Na_3Zr_2Si_2PO_{12}$ and doped NASICON. *J. Am. Ceram. Soc.* **2015**, *98*, 2902−2907.

(13) Zhang, Z.; Zhang, Q.; Shi, J.; Chu, Y. S.; Yu, X.; Xu, K.; Ge, M.; Yan, H.; Li, W.; Gu, L.; Hu, Y.-S.; Li, H.; Yang, X.-Q.; Chen, L.; Huang, X. A self-forming composite electrolyte for solid-state sodium battery with ultralong cycle life. *Adv. Energy Mater.* **2017**, *7*, 1601196−1601207.

(14) Zhang, Z.; Xu, K.; Rong, X.; Hu, Y.-S.; Li, H.; Huang, X.; Chen, L. $Na_{3.4}Zr_{1.8}Mg_{0.2}Si_2PO_{12}$ filled poly(ethylene oxide)/$Na(CF_3SO_2)_2N$ as flexible composite polymer electrolyte for solid-state sodium batteries. *J. Power Sources* **2017**, *372*, 270−275.

(15) Zhang, Z.; Zhang, Q.; Ren, C.; Luo, F.; Ma, Q.; Hu, Y.-S.; Zhou, Z.; Li, H.; Huang, X.; Chen, L. A ceramic/polymer composite solid electrolyte for sodium batteries. *J. Mater. Chem. A* **2016**, *4*, 15823−15828.

(16) Ma, Q.; Guin, M.; Naqash, S.; Tsai, C.-L.; Tietz, F.; Guillon, O. Scandium-substituted $Na_3Zr_2(SiO_4)_2(PO_4)$ prepared by a solution-assisted solid-state reaction method as sodium-ion conductors. *Chem. Mater.* **2016**, *28*, 4821−4828.

(17) Hong, H. Y. P. Crystal structures and crystal chemistry in the system $Na_{1+x}Zr_2Si_xP_{3-x}O_{12}$. *Mater. Res. Bull.* **1976**, *11*, 173−182.

(18) Goodenough, J. B.; Hong, H. Y. P.; Kafalas, J. A. Fast Na^+-ion transport in skeleton structures. *Mater. Res. Bull.* **1976**, *11*, 203−220.

(19) Hou, W.; Guo, X.; Shen, X.; Amine, K.; Yu, H.; Lu, J. Solid electrolytes and interfaces in all-solid-state sodium batteries: Progress and perspective. *Nano Energy* **2018**, *52*, 279−291.

(20) Gao, H.; Xue, L.; Xin, S.; Park, K.; Goodenough, J. B. A plastic−crystal electrolyte interphase for all-solid-state sodium batteries. *Angew. Chem., Int. Ed.* **2017**, *56*, 5541−5545.

(21) Shannon, R. D. Revised effective ionic radii and systematic studies of interatomie distances in halides and chaleogenides. *Acta Crystallogr., Sect. A: Cryst. Phys., Diffr., Theor. Gen. Crystallogr.* **1976**, *32*, 751−767.
(22) Zhang, Z.; Zou, Z.; Kaup, K.; Xiao, R.; Shi, S.; Avdeev, M.; Hu, Y.-S.; Wang, D.; He, B.; Li, H.; Huang, X.; Nazar, L. F.; Chen, L. Correlated migration invokes higher Na^+-ion conductivity in NaSICON-type solid electrolytes. *Adv. Energy Mater.* **2019**, *9*, 1902373−1902386.
(23) Tseng, C.-F.; Chen, P.-H.; Lin, P.-A. Low temperature sintering and microwave dielectric properties of $Zn_{0.5}Ti_{0.5}NbO_4$ ceramics with ZnO additive for LTCC applications. *J. J. Alloys Compd.* **2015**, *632*, 810−815.
(24) Ma, Q.; Tsai, C.-L.; Wei, X.-K.; Heggen, M.; Tietz, F.; Irvine, J. T. S. Room temperature demonstration of a sodium superionic conductor with grain conductivity in excess of 0.01 S cm^{-1} and its primary applications in symmetric battery cells. *J. Mater. Chem. A* **2019**, *7*, 7766−7776.
(25) Lee, H.; Dellatore, S. M.; Miller, W. M.; Messersmith, P. B. Mussel-inspired surface chemistry for multifunctional coatings. *Science* **2007**, *318*, 426−430.
(26) Sun, T.; Li, Z.-j.; Wang, H.-g.; Bao, D.; Meng, F.-l.; Zhang, X.-b. A biodegradable polydopamine-derived electrode material for high-capacity and long-life lithium-ion and sodium-ion batteries. *Angew. Chem., Int. Ed.* **2016**, *55*, 10662−10666.
(27) Hu, Z.; Zhu, Z.; Cheng, F.; Zhang, K.; Wang, J.; Chen, C.; Chen, J. Pyrite FeS_2 for high-rate and long-life rechargeable sodium batteries. *Energy Environ. Sci.* **2015**, *8*, 1309−1316.
(28) Noguchi, Y.; Kobayashi, E.; Plashnitsa, L. S.; Okada, S.; Yamaki, J.-i. Fabrication and performances of all solid-state symmetric sodium battery based on NASICON-related compounds. *Electrochim. Acta* **2013**, *101*, 59−65.
(29) Kehne, P.; Guhl, C.; Ma, Q.; Tietz, F.; Alff, L.; Hausbrand, R.; Komissinskiy, P. Sc-substituted Nasicon solid electrolyte for an all-solid-state Na_xCoO_2/Nasicon/Na sodium model battery with stable electrochemical performance. *J. Power Sources* **2019**, *409*, 86−93.
(30) Lalère, F.; Leriche, J. B.; Courty, M.; Boulineau, S.; Viallet, V.; Masquelier, C.; Seznec, V. An all-solid state NASICON sodium battery operating at 200 °C. *J. Power Sources* **2014**, *247*, 975−980.

https://dx.doi.org/10.1021/acsenergylett.0c01432
ACS Energy Lett. 2020, 5, 2835−2841